Journal of Advanced Ceramics https://mc03.manuscriptcentral.com/jacer
J Adv Ceram 2025, **14**: 9221167

https://doi.org/10.26599/JAC.2025.9221167

Research Article

Ultra-high energy harvester performance in KNN-based textured piezoceramics via multiscale reconfiguration design

Caixia Zhu, Jin Qian✉, Luomeng Tang, Cheng Shi, Bo Shen, Jiwei Zhai✉

Key Laboratory of Advanced Civil Engineering Materials of Ministry of Education, Functional Materials Research Laboratory, School of Materials Science and Engineering, Tongji University, Shanghai 201804, China.

✉ Corresponding authors.

E-mail: J. Qian, j_qian@tongji.edu.cn;

J. Zhai, apzhai@tongji.edu.cn

Received: July 6, 2025; Revised: August 15, 2025; Accepted: September 4, 2025

Abstract

The lower electromechanical performance of lead-free piezoelectric materials remains a critical bottleneck impeding their ability to replace lead-based materials in energy harvesting. To overcome this predicament, here, we propose a multiscale reconfiguration design to tailor the intricate coupling between structure and properties in (K,Na)NbO_3-based piezoelectric materials. The constructed multiphase coexistence, local structural heterogeneity, enhanced crystal anisotropy, and acceptor doping yield (K,Na)NbO_3-based ceramics with a harmonious balance between the piezoelectric coefficient and the dielectric constant. As a result, the (K,Na)NbO_3-based textured ceramics demonstrate exceptional piezoelectric properties, including a piezoelectric charge coefficient (d_{33}) of 551 pC N^{-1} and a piezoelectric voltage coefficient (g_{33}) of 54.2 mV m N^{-1}. The energy harvesting devices exhibit an ultra-high instantaneous output power (P_{out}) of 4.85 mW and an instantaneous output power density (P_D) of 70.2 μW mm^{-3}. This work provides valuable insights into the design and development of high-performance lead-free piezoelectric ceramics, and significantly advances the potential of (K,Na)NbO_3-based ceramics as viable replacements for Pb(Zr,Ti)O_3-based ceramics in energy harvesting applications.

Keywords: Lead-free piezoelectric ceramics; Piezoelectric energy harvester; Texturing engineering; Phase structure; Domain configuration

1 Introduction

Piezoelectric ceramics enable the mutual conversion of electrical and mechanical energy, equipping devices with energy conversion capabilities and supporting their extensive use in actuators, transducers, and energy harvesters [1-4]. Piezoelectric energy harvesters (PEH) offer a safe and environmentally friendly power source by efficiently transforming mechanical vibrations into electricity. They provide an alternative to traditional chemical batteries and facilitate the self-powering of microelectronic devices, including biomedical implants, aerospace equipment, and Internet of Things (IoT) nodes [5-6]. A significant challenge to the widespread adoption of IoT technology lies in the self-powering power demands of critical components, such as sensors and wireless transceivers.

The output power of PEH is critically influenced by the piezoelectric figure of merit (FOM), defined as FOM $= d_{33} \times g_{33}$, and $g_{33} = \frac{d_{33}}{\varepsilon_0 \times \varepsilon_r}$, where ε_r represents the relative dielectric constant, g_{33} denotes the piezoelectric voltage coefficient, ε_0 is the vacuum dielectric constant, and d_{33} is the piezoelectric charge coefficient [7]. Consequently, the development of high-power PEH requires not only a high d_{33} but also a low dielectric constant. $Pb(Zr,Ti)O_3$ (PZT)-based ceramics have dominated the piezoelectric ceramics market. However, lead's toxicity poses significant risks to both human health and the environment [8]. Therefore, there is an urgent need to develop high-performance lead-free alternatives. Among lead-free piezoelectrics, $(K,Na)NbO_3$ (KNN)-based ceramics have garnered significant attention due to their excellent overall performance [9]. For instance, textured KNN-based ceramics produced by Saito et al. using the reaction template grain growth (RTGG) technique exhibited a high d_{33} of 416 pC N^{-1}, sparking extensive research efforts [10]. However, d_{33} values around 400 pC N^{-1} remain inferior to those of commercial PZT-based ceramics, underscoring the need for performance optimization strategies. Simultaneously, the direct proportionality between d_{33} and ε_r presents challenges to improvement of g_{33} [7].

In KNN-based lead-free piezoelectric ceramics, multiphase coexistence can effectively reduce the free energy barrier, thereby enhancing piezoelectric performance. For example, Zhang et al. achieved

the orthorhombic (O) and tetragonal (T) phase coexistence at room temperature by constructing an O-T phase boundary, resulting in d_{33} ~ 510 pC N^{-1} [11]. Similarly, Shi et al. introduced the rhombohedral (R) phase atop the O/T phase, forming a novel R-O-T triphasic boundary (NPB) that delivers exceptional performance (d_{33} ~ 508 pC N^{-1}, Curie temperature (T_C) ~ 268 °C) [12]. Concurrently, texturing techniques can improve d_{33} while maintaining T_C. For instance, Lin et al. employed template TGG technology to induce highly oriented grains, increasing d_{33} from 185 to 435 pC N^{-1} in KNN ceramics while maintaining T_C ~ 360 °C [13]. Notably, local structural heterogeneity has garnered significant attention for their role in enhancing piezoelectric performance of ceramics [14]. Gao et al. demonstrated that dopants could induce the formation of high-density nanostructures. These structures significantly improve piezoelectric performance by modulating interfacial energy and flattening the energy barrier [14]. In addition, PEH demands a high electromechanical coupling coefficient (k_p) and a large g_{33}. It is reported that the acceptor doping (such as Fe, Cu, Mn, etc.) can induce a weak pinning effect that moderately suppresses ε_r while acting as a sintering aid to enhance densification and improve d_{33}. This approach promises the synergistic optimization of high d_{33} and g_{33} [15-16].

Here, based on the considerations above, as shown in **Fig. 1**, we designed (1-x)$(K_{0.5}Na_{0.5})(Nb_{0.938}Sb_{0.02}Ta_{0.04}Fe_{0.002})O_3$-$x(Bi_{0.5}Na_{0.5})HfO_3$ (x = 0.02, 0.03, 0.04, 0.05) ceramics through multiscale reconfiguration design. Crystal orientation was achieved using RTGG technology, while multiphase coexistence of R-O-T phases and local structural heterogeneity were constructed, enabling synergistic optimization of piezoelectric properties. Additionally, Fe acceptor doping was introduced to maintain a low ε_r, targeting outstanding comprehensive performance for KNN-based lead-free piezoelectric ceramics. Therefore, cross-scale structural collaborative optimization is achieved by integrating atomic-scale doping regulation, nanoscale construction of local structural heterogeneity, and microscale control over texture as well as mesoscopic multiphase coexistence. As a results, the textured KNN-based ceramics demonstrate outstanding piezoelectric properties (d_{33} ~ 551 pC N^{-1}, T_C ~ 321 °C, k_p ~ 77%, g_{33} ~ 54.2 mV m N^{-1}). PEH exhibited ultra-high instantaneous

output power (P_{out} ~ 4.85 mW) and instantaneous output power density (P_D ~ 70.2 μW mm^{-3}). These exceptional piezoelectric properties suggest that the T-3BNH ceramics can effectively replace lead-based piezoelectric ceramics in energy harvesting applications, showcasing their potential as a viable alternative to PZT piezoelectric ceramics.

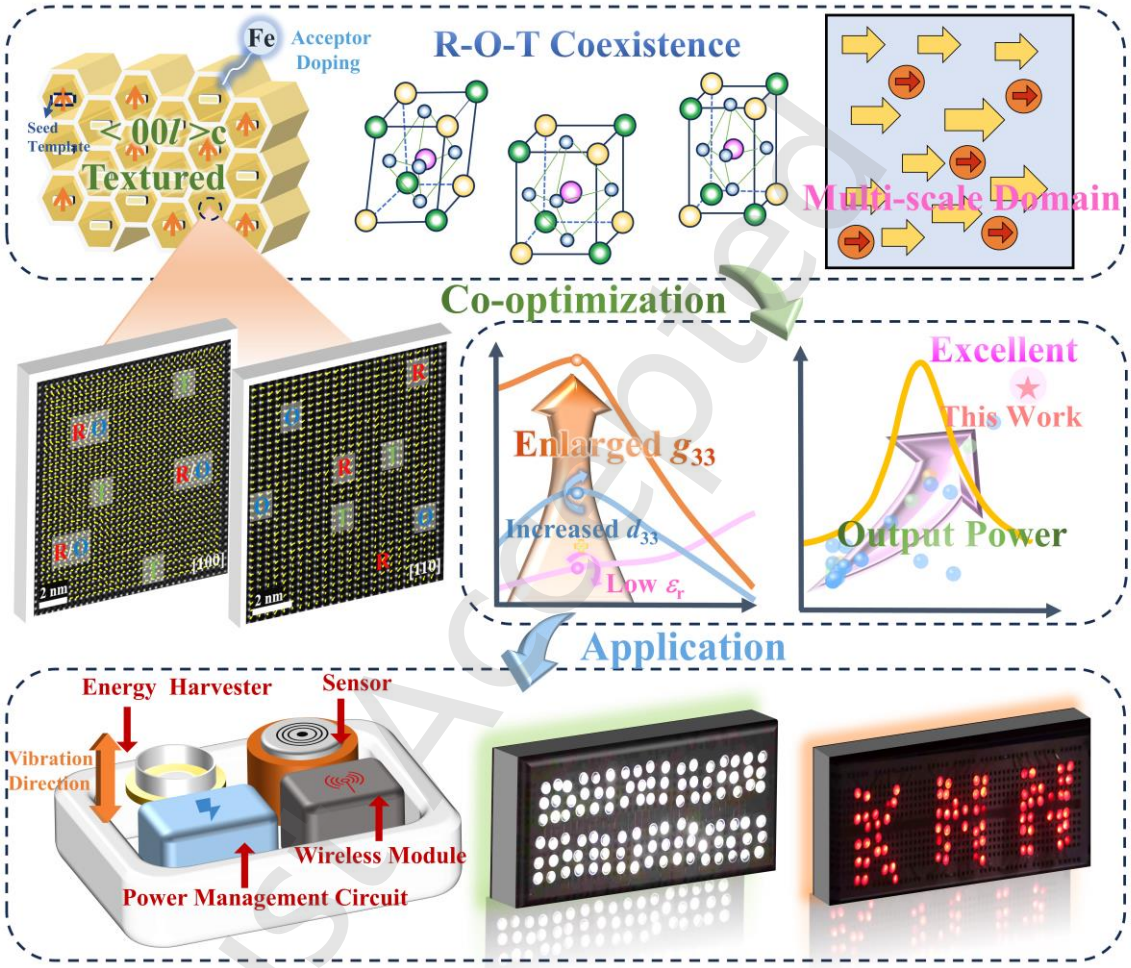

Fig. 1 Schematic diagram for ultra-high energy harvester performance in KNN-based textured piezoceramics via multiscale reconfiguration design.

2 Experimental Section

2.1 Sample Preparation

The quality of the template seed crystal directly determines the texture of piezoelectric ceramics. In this study, the textured ceramics were prepared using $NaNbO_3$ template (NN template), which has a high degree of compatibility with the KNN-based ceramic lattice. The NN template prepared by the

two-step molten salt method has a large length-to-diameter ratio, good dispersion, and no agglomeration (**Fig. S1**).

Random and textured ceramics of $(1-x)(K_{0.5}Na_{0.5})(Nb_{0.938}Sb_{0.02}Ta_{0.04}Fe_{0.002})O_3-xBi_{0.5}Na_{0.5}HfO_3$ (x = 0.02, 0.03, 0.04, 0.05) were prepared using conventional solid-state reaction and reaction template grain growth (RTGG) methods. The raw materials used were as follows: Nb_2O_5 (Aladdin, 99.98%), Na_2CO_3 (Aladdin, 99.8%), Bi_2O_3 (Alpha, 99.98%), Fe_2O_3 (Aladdin, 99.99%), Ta_2O_5 (Aladdin, 99.99%), Sb_2O_3 (Aladdin, 99.99%), K_2CO_3 (Aladdin, 99.99 %), and HfO_2 (Aladdin, 99.99%). For each batch, 20 g of materials were weighed according to the stoichiometric formula. The powders were mixed with 2/3 volume of anhydrous ethanol and ball-milled for 24 hours using 55 g of ZrO_2 ceramic balls. The resulting slurry was poured into a crystallizing dish, dried at 100 °C, and then pre-sintered at 850 °C for 5 hours. After pre-sintering, the powder underwent secondary ball milling for 12 hours followed by another drying step. The dried powder was granulated using 8 wt% polyvinyl alcohol (PVA) as a binder. Discs (12 mm diameter and 1 mm thickness) were pressed at 10 MPa and subjected to debinding at 600 °C for 10 hours. Finally, sintering was performed using a two-step method: heating to 1160-1200 °C, rapidly cooling to 1060-1100 °C, and holding at this temperature for 8-10 hours.

Textured ceramics were prepared using the RTGG method. Powder was mixed with 4 wt% NN templates and various organic solvents to prepare a tape-casting slurry. The well-mixed slurry was cast onto a carrier film and dried. The dried tapes were laminated into 12×12 mm square sheets via hot pressing, followed by binder removal. The two-step sintering method was then applied: heating to 1170-1210 °C, rapidly cooling to 1070-1110 °C, and holding for 8-10 hours to obtain textured ceramics.

2.2 Fabrication of piezoelectric energy harvester

The ceramics were fabricated into piezoelectric circular diaphragm (PCD) energy harvesters for experimental study. First, ceramics (~22 mm diameter) were prepared via the RTGG method described above. The sintered ceramics were then thinned to ~ 0.22 mm thickness. Silver electrodes (~21 mm diameter) were applied to both sides and annealed at 560 °C for 30 minutes. The samples were fully

poled under an AC electric field of 25 kV cm^{-1}. The proof mass (14 g), a poled ceramic disc, a studdle and wires were bonded onto a brass substrate and cured to form the PCD energy harvester. The harvester was mounted on a mechanical shaker for testing. Vibration frequency and amplitude (fixed as 4 V) were controlled using a signal generator (33220A, Agilent). The vibration shaker was operated at an acceleration of 9.8 m s^{-2}, as measured by an accelerometer. Real-time voltages across a load resistor were recorded using a digital oscilloscope.

2.3 Ex-situ structural characterization

The surface and cross-sectional microstructures of the ceramics were examined using scanning electron microscopy (SEM, HITACHI, TM4000Plus).

The room-temperature phase structure was analyzed by X-ray diffraction (XRD, Bruker D2 PHASER). Transmission electron microscopy (TEM) and atomic-resolution scanning transmission electron microscopy (STEM) samples were prepared by mechanical thinning, ultrasonic cutting, and argon-ion milling to electron transparency (30-50 nm thickness). Vertical piezoelectric response force microscopy (V-PFM) images were acquired using a piezoelectric response force microscope (PFM, Dimension Icon, Bruker, United States). Texture analysis was performed using electron backscatter diffraction (EBSD) pole figures and inverse pole figures. The Hitachi HF5000 TEM (200 kV, Japan) provided dark-field images for regional morphological analysis. Atomic-scale imaging was conducted on the Cs-corrected version of this microscope.

2.4 *In-situ* structural characterization

In-situ Temperature XRD: XRD patterns at different temperatures were acquired on an X-ray diffractometer (PA Nalytical Empyrean, Netherlands) equipped with a heating stage.

In-situ Electric Field XRD: Phase structures under applied electric fields (0-35 kV cm^{-1}, sample thickness ~ 0.3 mm) were examined using a custom-built in-situ electric field XRD sample holder. Semi-transparent gold electrodes, deposited via DC sputtering, were employed as the *in-situ* XRD tests under variable electric fields.

2.5 Electrical property characterization

The ceramics samples were mechanically polished to 0.5 mm thickness, and silver electrodes were applied to both sides. After firing the electrodes at 560 °C for 30 minutes, ferroelectric, dielectric, and electric field-induced strain properties were characterized. Characterization of polarization-electric field (*P*-*E*) loops and strain-electric field (*S*-*E*) loops was performed at a frequency of 10 Hz using a ferroelectric test system (Precision Premier II, Radiant Technologies). Subsequently, the specimens were poled under a direct current (DC) electric field of 25 kV cm^{-1} at room temperature. The piezoelectric coefficient (d_{33}) was then measured at room temperature using a quasi-static d_{33} meter (ZJ - 6A, Institute of Acoustics, CSA). A heating stage integrated with an Agilent E4980A LCR meter and Keithley 2410 source meter was employed to measure the temperature-dependent dielectric constants (ε_r-*T*) across 25 - 400 °C. The k_p was evaluated with an impedance analyzer (HP4294A, Agilent, United States).

3 Results and Discussion

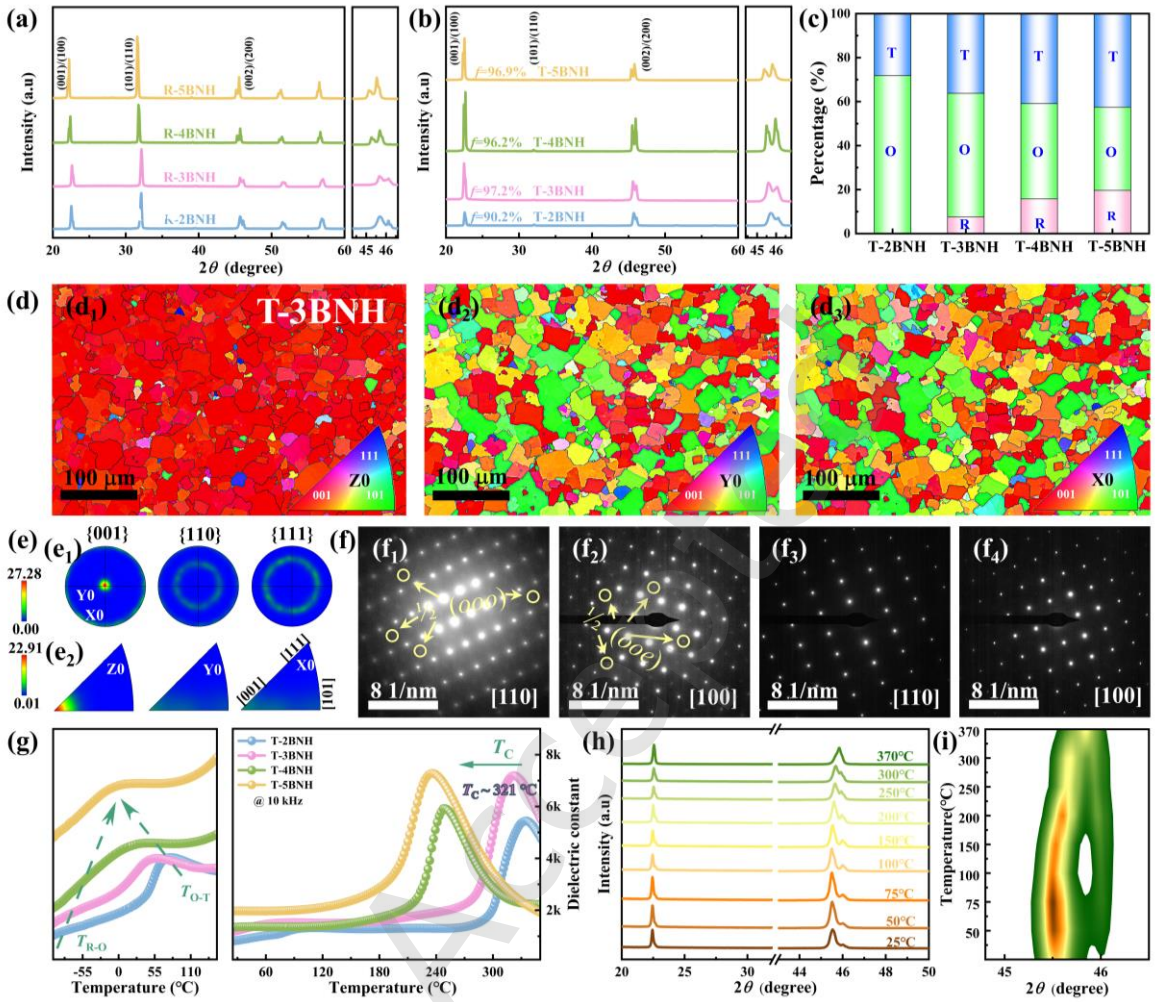

Fig. 2 XRD patterns of R-*x*BNH (**a**) and T-*x*BNH (**b**) ceramics. (**c**) Summary of XRD rietveld refinement patterns results for T-*x*BNH ceramics. Inverse pole figure maps of $<00l>_C$ textured T-3BNH ceramics along (**d1**) Z, (**d2**) Y and (**d3**) X-axis. (**e1**) Pole and (**e2**) inverse pole figure set of the T-3BNH ceramics. (**f1**) - (**f4**) SAED patterns of T-3BNH ceramics. (**g**) ε_r-*T* curves of T-*x*BNH ceramics. (**h**) - (**i**) *In-situ* variable temperature XRD for the T-3BNH ceramics.

In **Figs. S1** and **S2**, SEM characterization reveals distinct microstructural evolution with well-developed grain architectures in both random ceramics (marked as R-*x*BNH) and textured ceramics (marked as T-*x*BNH). The grain size in both types of ceramics progressively decreases with increasing BNH doping content, correlating with elevated configurational system entropy [17]. Notably, T-*x*BNH, prepared through the RTGG process, exhibits significant template-induced anisotropy, forming a

regular brick-like morphology. Furthermore, its overall grain size, ranging from 20-30 μm, remains larger than that of R-*x*BNH ceramics, owing to template nucleation sites facilitating grain growth [17]. To analyze the crystalline phase, comparative XRD patterns of R-*x*BNH and T-*x*BNH ceramics were obtained and are presented in **Figs. 2a-b**. All ceramics display a single perovskite-type structure with no detectable secondary phases, indicating that BNH is fully dissolved into the KNN perovskite lattice. The (002) to (200) peak ratios for R-*x*BNH and T-*x*BNH ceramics range between 1:2 and 2:1, signifying the coexistence of T and O phases in KNN-*x*BNH [19]. With increasing BNH concentration, both R-*x*BNH and T-*x*BNH ceramics show analogous evolution in their 45° diffraction profiles: a systematic intensification of the (200) reflection and attenuation of the (002) peak, suggesting a gradual increase in the T phase and a corresponding reduction in the O phase. Further rietveld refinement of XRD patterns for T-*x*BNH ceramics (**Fig. 2c)** indicates that KNN-2BNH ceramics display a coexistence of O-T phases, while the introduction of BNH contributes to the emergence of an R phase. As the BNH content increases, the proportion of the R phase incrementally rises from 0 % to 19.6 %, with all error factor R_p is less than 5.

Quantitative phase analysis in **Figs. S3**-**S5** highlights that R-*x*BNH and T-*x*BNH ceramics with identical compositions exhibit comparable phase fraction distributions, confirming that the texturing process does not significantly alter the phase structure but rather induces grain orientation. Comparative XRD analysis further underscores pronounced enhancement in the $<00l>_C$ diffraction intensity for T-*x*BNH compared to R-*x*BNH, indicative of superior crystallographic texture development [8]. The Lotgering factor $f_{(00l)}$, used to quantify the degree of texturing degree in KNN-based piezoelectric ceramics, equals 1 for completely oriented ceramics and 0 for randomly oriented ones [20]. All T-*x*BNH specimens demonstrate significantly high $f_{(00l)}$ orientation parameters exceeding 90%, with the T-3BNH variant showing exceptional texturing characterized by a maximum orientation factor of 97.2 %. To validate the textured degree observed in the XRD analysis, EBSD was employed (**Figs. 2d**-**e**). The analysis of the inverse pole figure (**Figs. 2d$_1$-d$_3$**) and inverse pole/pole

figure sets (**Figs. 2e$_1$-e$_2$**) reveals that the grain orientation of polycrystalline ceramics T-3BNH is non-random, exhibiting a consistent regularity. Nearly all grains have their <00*l*>$_C$ direction aligned parallel to the Z-axis (perpendicular to the casting direction) rather than the X or Y axes. These findings confirm that T-3BNH possesses a strong <00*l*>$_C$ texture [21]. The observed multiphase coexistence and enhanced crystallographic anisotropy are anticipated to significantly enhance the performance of KNN-based piezoelectric ceramics [20, 22-23].

To further validate the existence of the R-O-T phase boundary, SAED and ε_r-*T* curves were analyzed. **Fig. 2f** presents the SAED results for T-3BNH. Notably, in the **Fig. 2f$_1$** region, the SAED image obtained using the [110] zone axis displays a distinct 1/2 (*ooo*) superstructural reflection, indicating the R phase [23]. Meanwhile, in the **Fig. 2f$_2$** region, the SAED image obtained using the [100] zone axis exhibits a distinct 1/2 (*ooe*) superstructural reflection, signifying the O phase [24]. **Figs. 2f$_3$** and **f$_4$** showcase SAED results captured in the same region along the [100] and [110] zone axes. No superstructural reflection spots corresponding to the O and R phases were observed, confirming the presence of the T phase. These SAED observations conclusively demonstrate that the phase structure of T-3BNH features the coexistence of R, O, and T phases. The ε_r-*T* curves for T-*x*BNH are shown in **Figs. 2g-S6**. With increasing BNH doping, both the T_C, and the phase transition temperatures ($T_{R\text{-}O}$ and $T_{O\text{-}T}$) progressively shift toward room temperature, ultimately forming the $T_{R\text{-}O\text{-}T}$ phase boundary (NPB). The ε_r-*T* curves for R-*x*BNH exhibit a similar trend (**Fig. S7**), confirming that the texturing engineering does not significantly alter the phase structure of the ceramics, which aligns with the XRD results. In the low-temperature region, multi-frequency ε_r-*T* curves for T-*x*BNH are displayed in **Fig. S6**. These curves indicate that as BNH content increases, the dielectric anomaly peaks of $T_{R\text{-}O}$ and $T_{O\text{-}T}$ broaden, demonstrating that higher BNH content introduces more relaxation elements within the ceramics (including smaller domains and more localized random fields) [25]. Additionally, the phase structure of T-3BNH ceramics was observed using *in-situ* temperature-variable XRD (**Figs. 2h-i**). As temperature changes, a distinct abrupt transition zone is observed, corresponding to $T_{O\text{-}T}$ and T_C,

respectively, which is consistent with the findings from ε_r-*T* curves. The transformation from O/T two-phase coexistence to R-O-T three-phase coexistence reduce the polarization-flipping barrier in ceramics, thereby promoting polarization flipping. This, in turn, enhances the piezoelectric and ferroelectric properties of the ceramics [26].

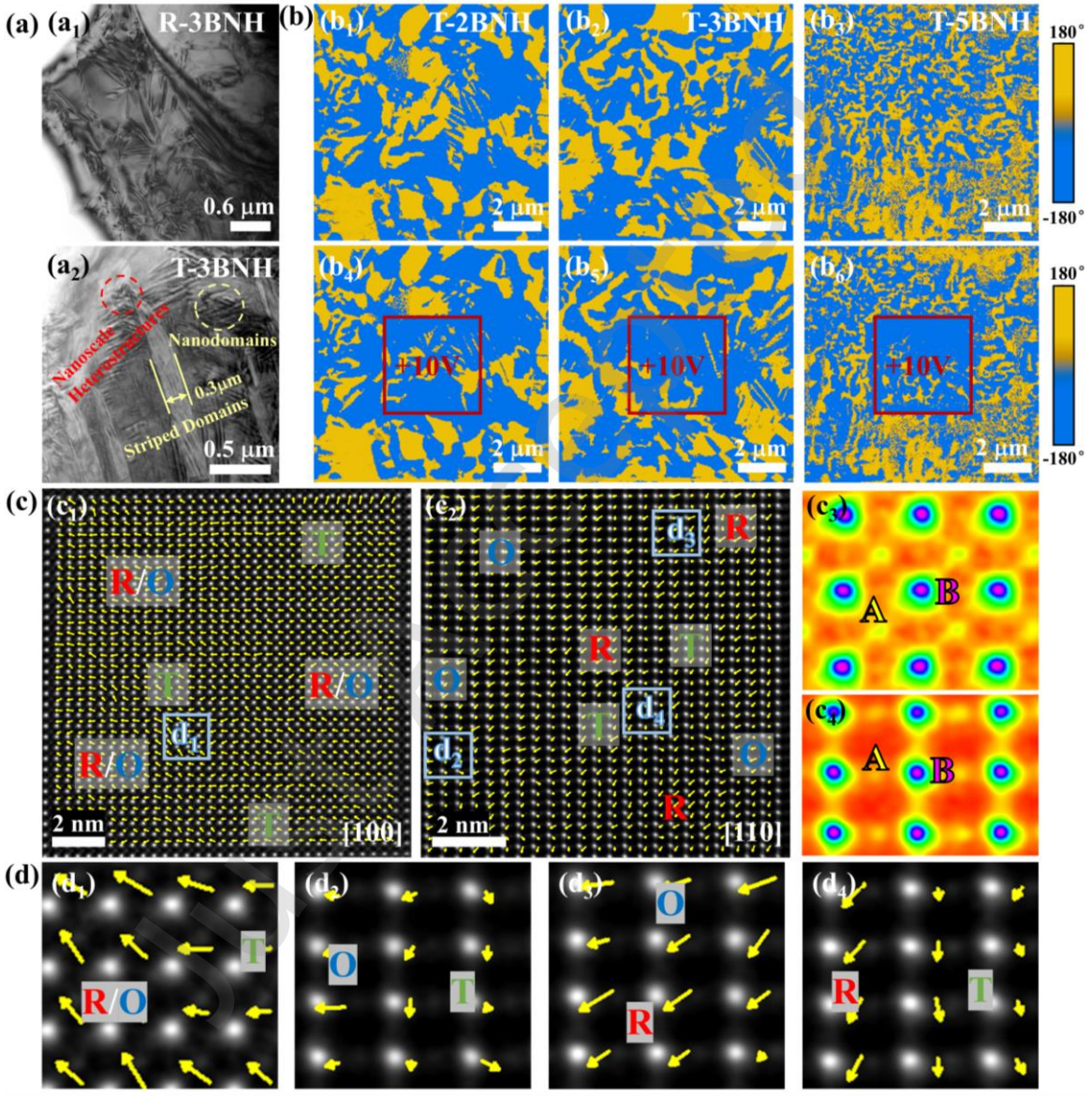

Fig. 3 TEM images for (**a1**) R-3BNH ceramics and (**a2**) T-3BNH ceramics. PFM phase images and PFM phase images after poling with 10 V voltage of T-2BNH (**b1, b4**), T-3BNH (**b2, b5**) and T-5BNH (**b3, b6**). Enlarged atomic-resolution HAADF-STEM polarization vector image along (**c1**) [100] and (**c2**) [110] for T-3BNH, respectively, superimposed with a map of atom polarization vectors. Schematic

projection of the unit cell along (**c**$_3$) [100] and (**c**$_4$) [110]. (**d**$_1$) - (**d**$_4$) Amplified images of the local regions of the phase transitions extracted from (**c**$_1$) - (**c**$_2$).

In addition to the anisotropy of crystal and phase structures mentioned above, the domain structure plays a crucial role in influencing the polarization and piezoelectric properties [27-29]. To investigate the domain structure, PFM, TEM, and high-angle annular dark-field scanning transmission electron microscopy (HAADF-STEM) were utilized [30-32]. **Figs. 3a**, **S8**, and **S9** reveal the domain structures in R-3BNH and T-3BNH, respectively. Both samples exhibit diverse domain structures among different grains, including various angles (109 °, 120 °, 180 °) and varying sizes, such as submicron stripe domains with widths of hundreds of nanometers, nanodomains (1-100 nm) and nanoscale heterostructures. Additionally, it can be observed that the domain size increases significantly following texture engineering, which correlates with changes in grain size [33].

The intrinsic piezoelectric properties of ceramics are theoretically positively correlated with domain size. While large-size domains exhibit high intrinsic piezoelectric properties, their substantial flipping energy barrier prevents effective flipping under an electric field. According to the typical domain theory $D \propto \sqrt{E_{\mathrm{DW}}}$, where D represents domain size and E_{DW} denotes domain wall energy, smaller domain sizes can reduce domain wall energy [34]. Excessive diffusion and miniaturization of domain structures can form a metastable system dominated by nanodomains. Despite the fast polarization response offered by such metastable structures, their thermodynamic instability induces spontaneous re-biasing, ultimately causing significant deterioration in macroscopic piezoelectric properties [35]. Consequently, while nanodomains flip easily, their intrinsic piezoelectric properties remain low. To overcome these challenges, constructing a multi-domain polar structure with local structural heterogeneity—embedding moderately nanoscale polar heterogeneity within a long-range ordered matrix—reduces the flipping barrier of the overall domain, thereby providing excellent ferroelectric and piezoelectric properties. **Figs. 3b** and **S10** present a PFM image of the T-*x*BNH and R-*x*BNH ceramics, illustrating the refinement and dispersion of domain sizes as the BNH content increases.

Three samples, T-2BNH, T-3BNH, and T-5BNH, were subjected to 10 V tip biases. The results reveal that the domain of T-2BNH sample was not fully switched under the electric field due to the larger overall domain size. In contrast, the domain structure dominated by dispersed small domains struggles to retain stability upon removal of the electric field. In the T-3BNH sample, the cross-scale configuration of nanodomains and large-size domains generates a multi-domain polar structure system with local structural heterogeneity. Within this system, nanoscale polar heterogeneous domains act as sources of easily switching polarization, while stable large-size domains maintain the long-range ordered polarization state, thereby stabilizing macroscopic piezoelectric performance. As a result, the optimal flipping and stability under the electric field are achieved.

A featured atomically resolved HAADF-STEM image, captured along the [100] zone axis, illustrates the polarization vector determined using 2D Gaussian peak fitting, derived from the shift of the B-site cation relative to its four neighboring A-site cations. **Fig. 3c1** highlights inhomogeneity in the $\delta_{\text{Nb-Na/K}}$ vector, with polarization vectors aligning along both the pseudo-cubic axis and diagonals, corresponding to the T and R/O symmetries [36]. However, distinguishing R and O phases from polarization vector projections along the [100] zone axis is infeasible, as their characteristics project identically on the (100) plane. To confirm the multiphase coexistence of R-O-T in this ceramics, the projection of the polarization vector on the [110] plane was analyzed, as depicted in the **Fig. 3c2**. **Figs. 3c3-c4** provide magnified HAADF-STEM images along with a schematic projection of the cell along the same axis. The local symmetry of ferroelectric materials is governed by their spontaneous polarization, arising from the relative displacement between positive and negative ion centers, thereby forming electric dipoles. The symmetry of the three phases (T, O, and R) in a perovskite piezoelectric structure is distinguishable by the spontaneous polarization (P_S) directions: [001], [110], and [111]. Analysis of displacement vector distributions along the [110] and [100] zone axes reveal large-scale, long-range ordered polarization regions associated with the R/O/T phases in the atomic local structure, further confirming the coexistence of R, O, and T phases in T-3BNH. The formation of the R/O/T

multiphase coexistence induces local polymorphic distortion, typically manifested as structural heterogeneity [19]. Consequently, short-range ordered polarization vector distributions related to R/O/T phases can be observed in T-3BNH ceramics, reinforcing the conclusion that T-3BNH ceramics exhibit local structural heterogeneity due to this multiphase coexistence. Magnified views further reveal polarization prone to flipping between regions with differing orientations (**Fig. 3d**). The low Gibbs free energy characteristic of this multiphase structure notably reduces polarization anisotropy, promoting an efficient polarization response under an external electric field.

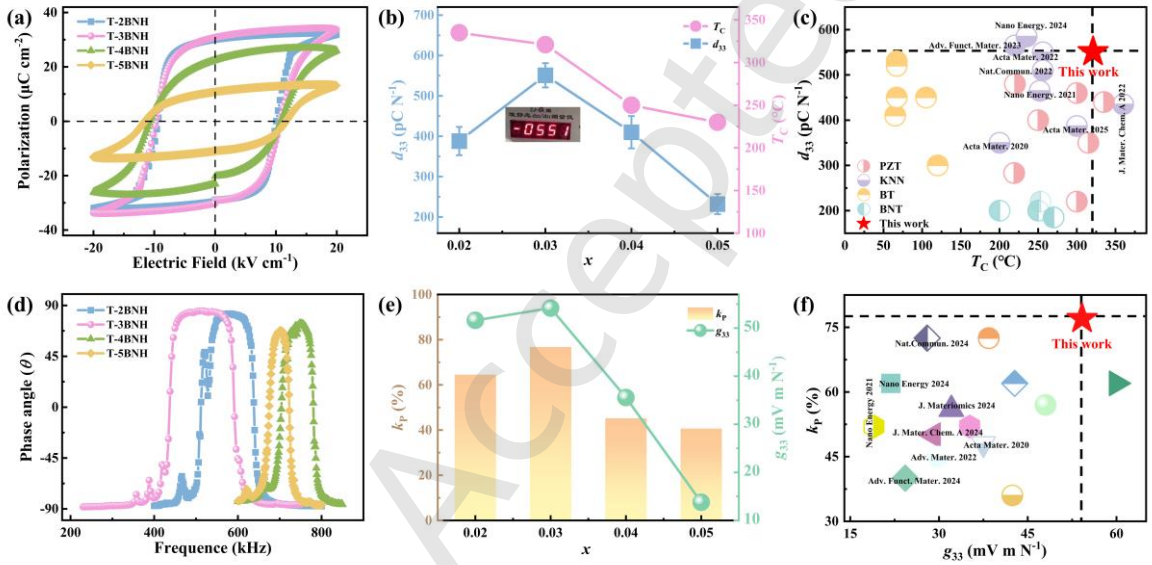

Fig. 4 (**a**) *P-E* loops of T-*x*BNH ceramics. (**b**) d_{33} and T_C value of T-*x*BNH ceramics. (**c**) Comprehensive performance comparison of T-3BNH with other piezoelectric ceramics, including T_C and d_{33}. (**d**) Phase angle θ against frequency of the T-*x*BNH ceramics measured at room temperature. (**e**) Comparison of k_p and g_{33} in T-*x*BNH ceramics. (**f**) Comprehensive performance comparison of the T-3BNH with other KNN-based piezoelectric ceramics, including k_p and g_{33}.

Figs. 4a and **S11** illustrate the *P-E* loops and *S-E* loops for R-*x*BNH and T-*x*BNH ceramics at 10 Hz. The results reveal that the remanent polarization (P_r) of textured ceramics is considerably higher than that of random ceramics. This indicates that the texturing treatment facilitates a more orderly alignment of electric dipoles following polarization under an external electric field, thereby enhancing

polarization efficiency and improving ferroelectric and piezoelectric performance [21]. For T-*x*BNH ceramics, P_r initially increases and then decreases as the BNH content raises, reaching optimal ferroelectricity at $x = 0.03$. This trend is attributed to the appropriate domain structure configuration within the ceramics. The piezoelectric properties of ceramics are closely tied to electric field-induced phase transitions. To explore the phase transformation process in T-3BNH ceramics under an applied electric field, *in-situ* electric field-dependent XRD analysis was performed. **Fig. S12** presents the *in-situ* electric field-dependent XRD patterns for T-3BNH ceramics. Under an external electric field, the intensity of the (002) peak progressively rises, while the (200) peak gradually diminishes, particularly near the coercive field. This signifies an electric field-induced sequential phase transition in the local structure, transitioning from the T phase to the O phase and subsequently to the R phase [25]. Following the removal of the voltage, the distorted diffraction peak in the T-3BNH ceramics exhibits minimal rebound, consistent with its highly saturated polarization state. Given the relationship $d_{33} \propto P_3 \times \varepsilon_r$(where P_3 represents the polarization along the polar axis, approximately corresponding to P_r), the piezoelectric properties of textured ceramics are markedly superior to those of random ceramics (**Fig. S13**).

In practical electromechanical applications, ideal piezoelectric ceramics must exhibit both high d_{33} and elevated T_C. However, in perovskite ferroelectrics, a typically constrained relationship exists between d_{33} and T_C [7,11,13,19,36-41]. **Fig. 4b** illustrates the d_{33} and T_C values for the T-*x*BNH ceramics. With increasing BNH content, d_{33} initially rises before declining, while T_C decreases consistently. T-3BNH ceramics demonstrate optimal piezoelectric properties, achieving $d_{33} \sim 551$ pC N^{-1} and $T_C \sim 321$ °C. This exceptional performance can be attributed to three primary factors: the optimized phase coexistence ratio of the ceramics R/O/T, suitable domain structure configurations, and enhanced crystallographic anisotropy induced by texturing. **Fig. 4c** highlights the correlation between d_{33} and T_C across various piezoelectric ceramics, showing that T-3BNH ceramics developed in this study achieve substantially improved d_{33} values while maintaining high T_C, enabling a broader

range of practical applications.

Additionally, the g_{33} serves as a critical performance parameter. In recent years, research has predominantly focused on d_{33} improvement, with relatively less attention to enhancing g_{33}. Nevertheless, the g_{33} coefficient is crucial for piezoelectric devices, particularly in energy harvesting applications. In PEH, higher k_p values are directly linked to greater energy conversion efficiency of piezoelectric ceramics under resonant conditions, thereby improving energy harvesting performance. **Figs. 4d** and **S14** reveal the phase angle and frequency dependence across different components, with all ceramic samples exhibiting phase angles nearing 90 °, indicating adequate polarization. **Fig. 4e** presents k_p and g_{33} values for T-*x*BNH ceramics, among which T-3BNH records the highest k_p (77 %) and g_{33} (54.2 mV m N^{-1}). As the increase of x, k_p first increased and then decreased. This phenomenon is related to changes in domain structure [13,19]. The elevated g_{33} of T-3BNH is attributed not only to its increased d_{33} values but also to the acceptor doping in this study, which reduces the dielectric constant to a certain extent [17,19,25,38,42-50]. **Fig. 4f** compares the g_{33} and k_p properties achieved in this research with those of other lead-free piezoelectric ceramics, demonstrating the highly competitive performance of this work. These results underscore the significant potential of T-3BNH ceramics for lead-free energy harvesting applications.

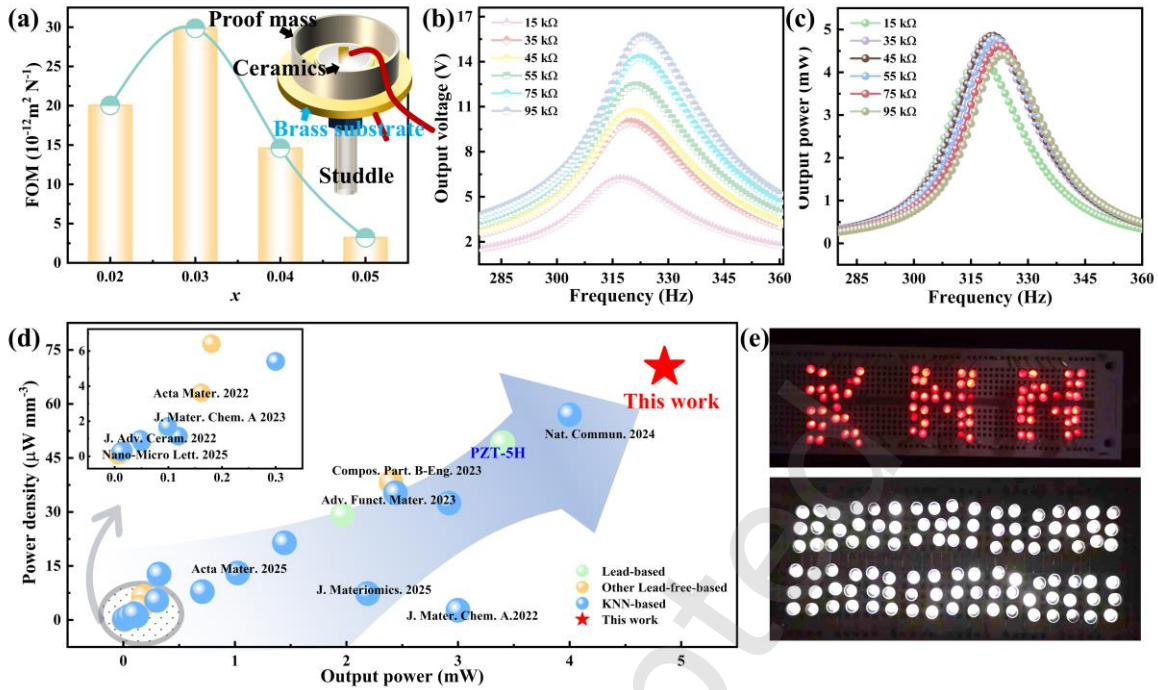

Fig. 5 (**a**) FOM values for T-*x*BNH ceramics. (**b-c**) V_{out} and P_{out} of PEH of T-3BNH ceramics at different vibration frequency/load resistance. (**d**) The output power and power density comparison of the PEH with other lead-free/lead-based piezoelectric harvesters. (**e**) The real time lighting photo of light emitting diodes (LEDs) driven by the T-3BNH ceramics PEH.

In the development of high-performance lead-free piezoelectric ceramics, device design and performance evaluation are critical. To verify the feasibility of the synthesized high-performance T-3BNH ceramics for electromechanical energy conversion, a PEH was fabricated as a model system for corresponding research. A schematic diagram of the energy-harvesting unit is presented in **Fig. 5a**. As illustrated in **Fig. S15**, a sintered, large-size T-3BNH round ceramics sheet (22 mm in diameter and 0.22 mm in thickness) was integrated into a PCD PEH. The energy-harvesting measurements were performed using the electrical circuit depicted in **Fig. S16**. **Fig. 5a** highlights the FOM of T-*x*BNH ceramics, showing that T-3BNH achieves an optimal FOM value of approximately 29.98× 10^{-12} m^2 N^{-1}. This performance is comparable to that of commercial lead-based piezoelectric materials (PZT-4: 6.47 × 10^{-12} m^2 N^{-1}) [51].

Figs. 5b-c illustrate the output voltage (V_{out}) and output power (P_{out}) of the PEH based on T-3BNH

ceramics as functions of vibration frequency and load resistance. The results indicate that the T-3BNH ceramics PEH achieves maximum instantaneous V_{out} and P_{out} values of approximately 15.7 V and 4.85 mW, respectively, under matched load resistance and optimal vibration frequency, yielding a power density (P_D) of up to ~70.2 μW mm^{-3}. **Fig. 5d** compares the P_{out} and P_D of various PEHs fabricated with lead-free and lead-based piezoelectric ceramics [13,25,36,43-47,52-65]. Notably, the P_{out} and P_D of the T-3BNH ceramics PEH surpass those of most PEHs made with lead-free piezoelectric ceramics and are comparable to those of PEHs using commercial PZT-5H lead-based piezoelectric ceramics. **Fig. 5e** illustrates the illumination of a PEH composed of T-3BNH ceramics under matched load resistance and optimal vibration frequency. At the optimal vibration frequency of 320 Hz, the T-3BNH ceramics PEH is capable of effortlessly lighting up hundreds of bulbs. This ultra-high P_{out} and P_D exhibited by the T-3BNH ceramics PEH, underscoring its remarkable potential for applications in electromechanical energy conversion.

4 Conclusions

In summary, this study achieved exceptional piezoelectric energy harvesting performance in KNN-based ceramics through multiscale structural engineering. By simultaneously regulating texture, phase coexistence (R-O-T), and domain structure, we induced local structural heterogeneity and enhanced crystallographic anisotropy. This synergistic approach yielded outstanding piezoelectric properties (d_{33} ~ 551 pC N^{-1}, k_p ~ 77%). Simultaneously, Fe acceptor doping was employed to maintain a low dielectric constant, and a fine balance between the piezoelectric coefficient and the dielectric constant was achieved, resulting in a high g_{33} (~ 54.2 mV m N^{-1}). Consequently, the optimized T-3BNH ceramics demonstrated ultra-high device performance (P_{out} ~ 4.85 mW, P_D ~ 70.2 μW mm^{-3}). This research sheds light on the structure-property relationships in KNN-based piezoelectric ceramics and offers valuable insights for the design and fabrication of high-performance lead-free piezoelectric materials and devices tailored for energy harvesting applications.

Availability of data and materials:

The data that support the findings of this study are available from the corresponding author upon reasonable request.

Competing interests

The authors have no competing interests to declare that are relevant to the content of this article.

Founding

This word is sponsored by National Natural Science Foundation of China (52032007), and Natural Science Foundation of Shanghai (25ZR1404008).

Author contributions

Conceptualization: Caixia Zhu, Jin Qian, Jiwei Zhai; **Investigation**: Caixia Zhu, Jin Qian; **Software**: Caixia Zhu, Luomeng Tang, Cheng Shi, Bo Shen; **Data curation**: Caixia Zhu, Luomeng Tang, Cheng Shi, Bo Shen; **Writing - original draft preparation**: Caixia Zhu; **Writing - review and editing**: Jin Qian, Jiwei Zhai; **Funding acquisition**: Jin Qian, Jiwei Zhai; **Supervision**: Jiwei Zhai.

Electronic Supplementary Material (ESM)

Supplementary material, including SEM images, XRD Rietveld refinement patterns, ε_r-T curves, TEM images, PFM phase images, P-E loops, S-E loops, *in situ* electric field XRD patterns, and plots of phase angle θ against frequency, is available in the online version of this article.

References

[1] Lv X, Zhu JG, Xiao DQ, *et al*. Emerging new phase boundary in potassium sodium-niobate based ceramics. *Chem Soc Rev* 2020, **49**: 671-707.

[2] Huan Y, Zhang XF, Han TX. Research progress on high-power and high-performance perovskite-type piezoelectric ceramics. *China Powder Sci Technol* 2025, **31**: 1-22.

[3] Qian J, Liu Y, He LQ, *et al*. Topological bubble domain engineering for high strain response. *Sci Adv* 2025, **11**: eadw8840.

[4] Liu Q, Pan E, Liu FC, *et al*. (K,Na)NbO_3-based lead-free ceramics with enhanced temperature-stable piezoelectricity and efficient red luminescence, *J Adv Ceram* 2023, **12**: 373-385.

[5] Song H-C, Kim S-W, Kim HS, *et al*. Piezoelectric energy harvesting design principles for materials and structures: Material figure-of-merit and self-resonance tuning. *Adv Mater* 2020, **32**: 2002208.

[6] Wen QB, Qu FM, Yu ZJ, *et al*. Si-based polymer-derived ceramics for energy conversion and storage, *J Adv Ceram* 2022, **11**: 197-246.

[7] Zeng SR, Zou JZ, Song M, *et al*. The mechanism for the enhanced piezoelectricity, dielectric property and thermal stability in (K,Na)NbO_3 ceramics. *Acta Mater* 2025, **287**: 120801.

[8] Zhu LF, Liu D, Shi XM, *et al*. Ultrahigh piezoelectric performances of (K,Na)NbO_3 based ceramics enabled by structural flexibility and grain orientation. *Nat Commun* 2025, **16**: 901.

[9] Wang BQ, Geng HF, Zheng ZP, *et al*. Giant electric field-induced strain with high temperature-stability in textured KNN-based piezoceramics for actuator applications. *Adv Funct Mater* 2023, **33**: 2214643.

[10] Saito Y, Takao H, Tani T, *et al*. Lead-free piezoceramics. *Nature* 2004, **432**: 84-87.

[11] Zhang M-H, Shen C, Zhao CH, *et al*. Deciphering the phase transition-induced ultrahigh piezoresponse in (K,Na)NbO_3-based piezoceramics. *Nat Commun* 2022, **13**: 3434.

[12] Shi CY, Ma J, Wu J, *et al*. Coexistence of excellent piezoelectric performance and high curie temperature in KNN-based lead-free piezoelectric ceramics. *J Alloys Compd* 2020, **846**: 156245.

[13] Lin JF, Cao YB, Zhu K, *et al*. Ultrahigh energy harvesting properties in temperature-insensitive eco-friendly high-performance KNN-based textured ceramics. *J Mater Chem A* 2022, **10**: 7978-7988.

[14] Gao XY, Cheng ZX, Chen ZB, *et al*. The mechanism for the enhanced piezoelectricity in multi-elements doped (K,Na)NbO_3 ceramics. *Nat Commun* 2021, **12**: 881.

[15] Cheng YT, Guan SY, Wang Q, *et al*. Mechanism and application of lead-free KNN-based ceramics with superior piezoelectricity. *J Eur Ceram Soc* 2024, **44**: 6978-6986.

[16] Zhang ZD, Shang XZ, Liu X, *et al*. Achieving excellent mechanical and electrical properties in transition metal oxides and rare earth oxide-doped KNN-based piezoceramics. *J Am Ceram Soc* 2024, **107**: 5923-5938.

[17] Hua Y, Qian J, Yang YX, *et al*. Broad temperature plateau for high piezoelectric coefficient by embedding PNRs in singe-phase KNN-based ceramics. *Adv Funct Mater* 2024, **35**: 2414348.

[18] Xu LH, Lin JF, Yang YX, *et al*. Ultrahigh thermal stability and piezoelectricity of lead-free KNN-based texture piezoceramics. *Nat Commun* 2024, **15**: 9018.

[19] Liu Y, Fan JH, Qi XD, *et al*. Adaptive ferroelectric states in KNN-based piezoceramics: Unveiling the mechanism of enhancing piezoelectric properties through multiple phase boundary engineering. *Nano Energy* 2024, **128**: 109972.

[20] Yan YK, Geng LD, Liu HR, *et al*. Near-ideal electromechanical coupling in textured piezoelectric ceramics. *Nat Commun* 2022, **13**: 3565.

[21] Yang S, Li JL, Liu Y, *et al*. Textured ferroelectric ceramics with high electromechanical coupling factors over a broad temperature range. *Nat Commun* 2021, **12**: 1414.

[22] Li JL, Qu WB, Daniels J, *et al*. Lead zirconate titanate ceramics with aligned crystallite grains. *Science* 2023, **380**: 87-93.

[23] Yang HR, Tang LM, Han SP, *et al*. Ultra-stable thermal piezoelectricity up to 200 °C in high-performance KNN-based textured piezoceramics. *Adv Funct Mater* 2025, **36**: 2507702.

[24] Yamada H, Matsuoka T, Kozuka H, *et al*. Improvement of the piezoelectric properties in (K,Na)NbO_3-based lead-free piezoelectric ceramic with two-phase co-existing state. *J Appl Phys* 2015, **117**: 214102.

[25] Lin JF, Qian J, Ge GL, *et al*. Multiscale reconfiguration induced highly saturated poling in lead-free piezoceramics for giant energy conversion. *Nat Commun* 2024, **1**: 2560.

[26] Sun X-X, Li RC, Yang ZW, *et al*. Modulating polarization rotation to stimulate the high piezocatalytic activity of (K,Na)NbO_3 lead-free piezoelectric materials. *Appl Catal B-Environ* 2022, **313**: 121471.

[27] Qian J, Ge GL, Yu ZY, *et al*. High temperature stable capacitive energy storage up to 320 °C in high-entropy dielectric thin film. *Nano Energy* 2025, **135**: 110651.

[28] Zou JZ, Wei TX, Song M, *et al*. Unveiling the origin of ultrahigh piezoelectricity in sb doped KNN based piezoceramics. *Adv Funct Mater* 2025, **36**: 2425080.

[29] Qian J, Yu ZY, Ge GL, *et al*. Topological vortex domain engineering for high dielectric energy storage performance. *Adv Energy Mater* 2023, **14**: 2303409.

[30] Liu WB, Zheng T, Zhou ZY, *et al*. Ultrahigh piezoelectricity and temperature stability in piezoceramics by synergistic design. *Nat Commun.* 2025, **16**: 1527.

[31] Zou JZ, Song M, Zhou X, *et al*. Enhancing piezoelectric coefficient and thermal stability in lead-free piezoceramics: Insights at the atomic-scale. *Nat Commun* 2024, **15**: 8591.

[32] Qian J, Lv PP, Ge GL, *et al*. Diffusosphere engineering in bnt-based multilayer heterogeneous film capacitors for high performance. *J Materiomics* 2025, **11**: 100931.

[33] Lv X, Wang X, Ma YC, *et al*. Temperature stability of perovskite-structured lead-free piezoceramics: Evaluation methods, improvement strategies, and future perspectives. *Mater Sci Eng R-Rep* 2024, **159**: 100793.

[34] Cao WW, Randall CA. Grain size and domain size relations in bulk ceramics ferroelectric materials. *J Phys Chem Solids* 1996, **57**: 1499-1505.

[35] Wang B, Li F, Chen L-Q. Inverse domain-size dependence of piezoelectricity in ferroelectric crystals. *Adv Mater* 2021, **33**: 2105071.

[36] Lin JF, Ge GL, Li JF, *et al*. Field-induced multiscale polarization configuration transitions of mesentropic lead-free piezoceramics achieving giant energy harvesting performance. *Adv Funct Mater* 2023, **33**: 2303965.

[37] Li P, Fu ZQ, Wang FF, *et al*. High piezoelectricity and stable output in $BaHfO_3$ and $(Bi_{0.5}Na_{0.5})ZrO_3$ modified $(K_{0.5}Na_{0.5})(Nb_{0.96}Sb_{0.04})O_3$ textured ceramics. *Acta Mater* 2020, **199**: 542-550.

[38] Xing J, Chen H, Jiang LM, *et al*. High performance $BiFe_{0.9}Co_{0.1}O_3$ doped KNN-based lead-free ceramics for acoustic energy harvesting. *Nano Energy* 2021, **84**: 105900.

[39] Li P, Huan Y, Yang WW, *et al*. High-performance potassium-sodium niobate lead-free piezoelectric ceramics based on polymorphic phase boundary and crystallographic texture. *Acta Mater* 2019, **165**: 486-495.

[40] Wu JG, Xiao DQ, Zhu JG. Potassium–sodium niobate lead-free piezoelectric materials: Past, present, and future of phase boundaries. *Chem Rev* 2015, **115**: 2559-2595.

[41] Watson BH, Brova MJ, Fanton M, *et al*. Textured Mn-doped PIN-PMN-PT ceramics: Harnessing intrinsic piezoelectricity for high-power transducer applications. *J Eur Ceram Soc* 2021, **41**: 1270-1279.

[42] Go S-H, Park S-J, Kim S-H, *et al*. [001]-texturing of $(K,Na)NbO_3$-based piezoceramics with a pseudocubic structure and their application to piezoelectric devices. *J Materiomics* 2024, **10**: 632-642.

[43] Liu D, Li J-R, Wang L, *et al*. Energy harvesting properties for potassium-sodium niobate piezoceramics through synergistic effect of phase structure and texturing engineering. *Ceram Int* 2025, **51**: 836-843.

[44] Chae S-J, Na J-W, Kim D-S, *et al*. Application of [001]-textured (K,Na)(Nb, Sb)O_3-$CaZrO_3$ thick films to piezoelectric energy harvesters. *Ceram Int* 2022 **48**: 18401-18414.

[45] Li P, Gao S, Lu GR, *et al*. Significantly enhanced piezoelectric temperature stability of KNN-based ceramics through multilayer textured thick films composite. *J Eur Ceram Soc* 2024, **44**: 3861-3868.

[46] Chae S-J, Lee G-S, Kim S-H, *et al*. Fabrication and physical properties of $Na(Nb_{1-x}Sb_x)O_3$ templates for the [001]-texturing of KNN-based ceramics. *J Alloys Compd* 2024, **993**: 174611.

[47] Ye G, Wade-Zhu J, Zou J, *et al*. Microstructures, piezoelectric properties and energy harvesting performance of undoped $(K_{0.5}Na_{0.5})NbO_3$ lead-free ceramics fabricated via two-step sintering. *J Eur Ceram Soc* 2020, **40**: 2977-2988.

[48] Zheng T, Wu JG. Electric field compensation effect driven strain temperature stability enhancement in potassium sodium niobate ceramics. *Acta Mater* 2020, **182**: 1-9.

[49] Li HJ, Chen N, Xing J, *et al*. Heterogeneous diffusion and remnant hardening with excellent electromechanical compatibility in alkaline niobate composites. *J Mater Chem A* 2025, **13**: 1923-1931.

[50] Liu Y-X, Qu WB, Thong H-C, *et al*. Isolated-oxygen-vacancy hardening in lead-free piezoelectrics. *Adv Mater* 2022, **34**: 2202558.

[51] Alkoy S. Piezoelectric hollow sphere transducers: The 'BBs'. Ph.D. Thesis. University Park (PA): The Pennsylvania State University, 1999.

[52] Zheng MP, Hou YD, Yan XD, *et al*. A highly dense structure boosts energy harvesting and cycling reliabilities of a high-performance lead-free energy harvester. *J Mater Chem C* 2017, **5**: 7862-7870.

[53] Huan Y, Wang XJ, Yang WY, *et al*. Optimizing energy harvesting performance by tailoring ferroelectric/relaxor behavior in KNN-based piezoceramics. *J Adv Ceram* 2022, **11**: 935-944.

[54] Wu JG, Shi HD, Zhao TL, *et al*. High-temperature $BiScO_3$-$PbTiO_3$ piezoelectric vibration energy harvester. *Adv Funct Mater* 2016, **26**: 7186-7194.

[55] Yue YG, Hou YD, Zheng MP, *et al*. High power density in a piezoelectric energy harvesting ceramics by optimizing the sintering temperature of nanocrystalline powders. *J Eur Ceram Soc* 2017, **37**: 4625-4630.

[56] Liu YC, Chang YF, Sun EW, *et al*. Significantly enhanced energy-harvesting performance and superior fatigue-resistant behavior in $[001]_c$-textured $BaTiO_3$-based lead-free piezoceramics. *ACS Appl Mater Interfaces* 2018, **10**: 31488-31497.

[57] Yan XD, Zheng MP, Sun SJ, *et al*. Boosting energy harvesting performance in $(Ba,Ca)(Ti,Zr)O_3$ lead-free perovskites through artificial control of intermediate grain size. *Dalton trans* 2018, **47**: 9257-9266.

[58] Yan XD, Zheng MP, Gao X, *et al*. Ultrahigh energy harvesting performance in lead-free piezocomposites with intragranular structure. *Acta Mater* **222**, 117450 (2022).

[59] Chae Y-G, Chae S-J, Go S-H, *et al*. Ultrahigh performance piezoelectric energy harvester using lead-free piezoceramics with large electromechanical coupling factor. *Int J Energy Res* 2023, **2023**, 1-20.

[60] Xi KB, Hou YD, Yu XL, *et al*. Optimizing output power density in lead-free energy-harvesting piezoceramics with an entropy-increasing polymorphic phase transition structure. *ACS Appl Mater Interfaces* 2023, **15**: 51330-51338.

[61] Zheng MP, Hou YD, Chao LM, *et al*. Piezoelectric KNN ceramics for energy harvesting from mechanochemically activated precursors. *J Mater Sci: Mater Electron* 2018, **29**: 9582-9587.

[62] Xi KB, Hou YD, Yu XL, *et al*. Diffuse multiphase coexistence renders temperature-insensitive lead-free energy-harvesting piezoceramics. *J Mater Chem A* 2023, **11**: 3556-3564.

[63] Wu Q, Zhang FQ, Wang B, *et al*. A lead-free KNN-based, co-fired multilayered piezoceramics energy harvester with a high output current and power. *J Materiomics* 2025, **11**: 100876.

[64] Shi C, Lin JF, Ge GL, *et al*. Design and manufacture of lead-free eco-friendly cement-based piezoelectric composites achieving superior piezoelectric properties for concrete structure applications. *Compos. Part B-Eng.* 2023, **259**: 110750.

[65] Xi KB, Guo JZ, Zheng MP, *et al*. Defect engineering with rational dopants modulation for high-temperature energy harvesting in lead-free piezoceramics. *Nano-Micro Lett* 2024, **17**: 55.